Universiteit
Antwerpen

This item is the archived peer-reviewed author-version of:

Mechanical behavior of ultrathin sputter deposited porous amorphous Al_2O_3 films

Reference:
van der Rest Astrid, Idrissi Hosni, Henry Frédéric, Favache Audrey, Schryvers Dominique, Proost Joris, Raskin Jean-Pierre, Van Overmeere Quentin, Pardoen Thomas.- Mechanical behavior of ultrathin sputter deposited porous amorphous Al_2O_3 films
Acta materialia - ISSN 1359-6454 - 125(2017), p. 27-37
Full text (Publisher's DOI): https://doi.org/10.1016/J.ACTAMAT.2016.11.037
To cite this reference: https://hdl.handle.net/10067/1389900151162165141

uantwerpen.be
Institutional repository IRUA

*Text only
Click here to download Text only: A_16_1663_van der Rest_revised_Text.docx Click here to view linked References

1
2
3
4
5
6
7
8
9
10
11
12
13
14
15
16
17
18
19
20
21
22
23
24
25
26
27
28
29
30
31
32
33
34
35
36
37
38
39
40
41
42
43
44
45
46
47
48
49
50
51
52
53
54
55
56
57
58
59
60
61
62
63
64
65

Mechanical behavior of ultrathin sputter deposited porous amorphous Al_2O_3 films

Astrid van der Rest[a], Hosni Idrissi[a,c], Frédéric Henry[a], Audrey Favache[a], Dominique Schryvers[c], Joris Proost[a], Jean-Pierre Raskin[b], Quentin Van Overmeere[a,+], Thomas Pardoen[a,*],

[a] *Institute of Mechanics, Materials and Civil Engineering (iMMC), Université catholique de Louvain, B-1348 Louvain-la-Neuve, Belgium*

[b] *Institute of Information and Communication Technologies, Electronics and Applied Mathematics (ICTEAM), Université catholique de Louvain, B-1348 Louvain-la-Neuve, Belgium*

[c] *EMAT, University of Antwerp, Groenenborgerlaan 171, B-2020 Antwerp, Belgium*

The determination of the mechanical properties of porous amorphous Al_2O_3 thin films is essential to address reliability issues in wear-resistant, optical and electronic coating applications. Testing the mechanical properties of Al_2O_3 films thinner than 200 nm is challenging, and the link between the mechanical behavior and the microstructure of such films is largely unknown. Herein, we report on the elastic and viscoplastic mechanical properties of amorphous Al_2O_3 thin films synthesized by reactive magnetron sputtering using a combination of internal stress, nanoindentation, and on-chip uniaxial tensile testing characterization, together with mechanical homogenization models to separate the effect of porosity from intrinsic variations of the response of the sound material. The porosity is made of voids with 2 to 30 nm diameter. The Young's modulus and hardness of the films decrease by a factor of two when the deposition pressure increases from 1.2 to 8 mTorr. The contribution of porosity was found to be small, and a change in the atomic structure of the amorphous Al_2O_3 matrix is hypothesized to be the main contributing factor. The activation volume associated to the viscoplastic mechanism is around 100 $\dot{A}^3$. Differences in the atomic structure of the films could not be revealed by electron diffraction, pointing to a minute effect of atomic arrangement on the elastic properties.

Keywords: amorphous alumina, thin films, mechanical properties, porosity, nanoindentation

*Corresponding author: Thomas Pardoen,
Tel: +32 10 47 24 17 - Fax : +32 10 47 40 28
e-mail : thomas.pardoen@uclouvain.be

[+] Present Address: PARC, A Xerox Company, 3333 Coyote Hill Road, Palo Alto CA 94304, USA

E-mail: astrid.vanderrest@uclouvain.be Tel: +32 10/47.30.59 Address: Place Sainte-Barbe 2, B-1348 Louvain-la-Neuve, Belgium.

1. Introduction

Amorphous Al_2O_3 thin films are used in a variety of applications owing to an advantageous combination of hardness, transparency and electrically-insulating properties [1]. Most Al_2O_3 films are porous either with closed pores when produced by sputtering, e-beam evaporation, atomic layer deposition (ALD), and anodic oxidation of Al in non-acidic electrolytes, or with open pores when processed by anodic oxidation in acidic electrolytes. Al_2O_3 films with closed porosity are used among others as wear-resistant coatings [2], as passivation layers in metal-oxide-semiconductor (MOS) devices [3] or in solar cells [4]. Al_2O_3 films with open porosity are used as surface coatings on Al in different kinds of devices including smartphones, storage devices, etc. [5], as templates for coatings with high surface area [6], or as templates for the synthesis of nanowires [7]. In all cases, the mechanical performances of the films are important to preserve functionality. For instance, sufficient bendability is required in flexible devices [8], while scratch resistance is a major concern for a wide range of coatings [9]. Another interest of studying Al_2O_3 layers stems from the use of thin Al layers in micro and nano devices. The Al is always covered by a native Al_2O_3 film due to the oxide high thermodynamic stability [10]. Due to the small thickness, the elastic behavior [11] as well as the plastic behavior [12, 13, 14] of the metallic layers is altered by the presence of the oxide, which can limit the mechanical strength of the functional layer in some applications [15]. Proper control and optimization of the mechanical properties of Al_2O_3 layers in general requires to characterize, understand and model the relationships between deposition conditions, structure and porosity, and the deformation and failure mechanisms. This general objective has been partially addressed in the literature.

The mechanical properties of Al_2O_3 films produced by vapor deposition have been characterized in a variety of earlier studies. Koski et al. [16] studied the influence of several

sputtering deposition parameters, including the cathodic voltage, sputtering gas pressure and substrate bias voltage, on the internal stress (measured ex-situ), density, nano-hardness and elastic modulus. The elastic modulus was found to decrease with increasing deposition pressure, but without clear underlying explanation. Surprisingly, the density was found to increase with deposition pressure, whereas the density of films deposited by sputtering generally decreases with pressure. Wang et al. [17] studied the effects of the substrate bias and magnetic trap on the film crystallinity, hardness and refractive index. Crystalline alumina had a larger hardness (~25 GPa) than amorphous alumina (~10 to 12 GPa). Moghal et al. [9] performed uniaxial fragmentation and nano-scratch tests and qualitatively compared the adhesion and strain-to-failure of films deposited using various sputtering configurations (direct current, radio frequency and high power impulse magnetron sputtering). Delayed failure of the layer is promoted by direct current sputtering configuration, when compared to the two other configurations. Most of the experimental work was performed so far on Al_2O_3 layers thicker than 200 nm, essentially to avoid substrate effects when performing nanoindentation tests to characterize the elastic and plastic behavior. Also note that nanoindentation is not adapted to test fracture properties except for very brittle materials. Our experience is that Al_2O_3 films do not crack under the sharp tip of a nanoindenter. Only a few recent works have looked at films thinner than 200 nm using advanced microtesting methods. For instance, the so-called “push-to-pull” tensile test method [18], was used to extract the tensile strength evolution of ALD alumina layers 100 to 10 nm thick, exhibiting a strong size dependent strengthening with values increasing from 3.5 GPa to 5.2 GPa. Baumert et al. [8] studied the fatigue degradation properties of ALD alumina using silicon micro-resonators. Mueller et al. [19] measured the fracture toughness of nanocrystalline alumina fibres, with grain size ~65 nm, using a nanoindenter to deflect chevron-notched type cantilever beams, leading to a fracture toughness equal to 2.3 ± 0.2 MPa $m^{1/2}$. The relationship between the

internal stress, stiffness and microstructure of amorphous alumina films was investigated by curvature-induced internal stress measurements [20]. Differences in internal stress for films thinner than 300 nm could not be related to the film microstructure. A comprehensive understanding of the relationship between the deposition conditions, the porosity and the mechanical properties, especially the plastic and fracture properties, in Al_2O_3 thin films is still missing in the literature.

The objective of this work is to contribute to a better understanding of the dependence of the effective and intrinsic mechanical properties of Al_2O_3 films, with thickness in the sub 200 nm range, on the microstructure, as controlled by the deposition conditions. This range is of interest for many applications listed earlier in this introduction. Reactive magnetron sputtering (RMS) is used to fabricate amorphous alumina with closed random porosity. The mechanical properties of interest are the internal stress, the elastic modulus, the hardness and the strain rate sensitivity, with an emphasis on the link with the porosity. Two advanced mechanical characterization methods are used in this study, i.e. the Multibeam Optical Stress Sensor (MOSS) [21] and the "lab-on-chip" technique [12, 22, 23], supplemented by more classical methods. The MOSS is employed to extract the internal stress evolution in the film, which is closely related to the microstructure of the film. Complementary measurements using ellipsometry provide the film porosity and roughness. Transmission Electron Microscopy (TEM) has been used to investigate the microstructure of the films. The elastic modulus is determined by using the "on-chip" uniaxial tensile test adapted for the characterization of oxide films, and compared to nanoindentation data. The "on-chip" uniaxial tests also provide the fracture stress and fracture strain. Nanoindentation provides information on the viscoplastic response of the Al_2O_3 thin films. All the data are analysed based on porous elasticity and plasticity mechanical models. Besides reporting novel measurements of fundamental quantities such as strain rate sensitivity and fracture stress of

freestanding Al_2O_3 films, one of the main conclusions of the work is that not only the porosity and hence the effective properties of the layer change with deposition conditions, but also the intrinsic stiffness and strength of the matrix material around the pores.

The outline of the paper is as follows. Section 2 describes the deposition and characterization methods, as well as the mechanical test procedures. Section 3.1 presents the results about the internal stress and microstructure evolution, which are discussed and related to the deposition pressure in section 4.1. Section 3.2 focuses on the results about the mechanical properties. The link between the microstructure and elastic properties is discussed in section 4.2, and the link between the microstructure, hardness and viscoplastic response in section 4.3.

2. Experimental Procedures

2.1. Deposition and characterization methods

Al_2O_3 films involving closed porosity were grown by DC magnetron sputtering, from an Al target (99.9995% purity), with a target to substrate distance equal to 12.2 cm. The films were deposited on 3-inch single crystal silicon wafers. The samples were sputtered at ambient temperature and at pressures ranging from 1.2 to 8 mTorr, under a current of 300 mA and 350 mA in Ar/O_2 gas mixtures. The sputtering rates were measured before deposition and kept constant, as indicated by the constant voltage obtained by adjusting the O_2 partial pressure. The initial O_2 partial pressure was determined prior to deposition by bias voltage versus O_2 partial pressure measurement. The selected O_2 partial pressure was the highest accessible to ensure stoichiometry of the Al_2O_3 before the voltage drop which indicates poisoning of the Al target.

Internal stress evolution was monitored in real time during deposition by measuring the change of curvature of the substrate (ΔK), see Fig. 1.a. The measurement is optical, by means of a Multibeam Optical Stress Sensor (MOSS), using the calibration from [21]. The average internal stress $< \sigma_f >$ in the layer was extracted from the substrate curvature change using the Stoney equation:

$$< \sigma_f > h_f = \left(\frac{Y_f}{1-\nu_f}\right)\frac{h_s^2}{6}\Delta K, \tag{1}$$

where Y_f, ν_f and $h_{f\ or\ s}$ are Young's modulus, Poisson ratio and thickness of the substrate (*s*) or film (*f*), respectively.

The refractive index, porosity, thickness and roughness of the films were obtained ex-situ by ellipsometry, following the procedure proposed by Aspnes [24]. The dielectric function spectra of the films deposited on Si substrates were obtained over the range 190 nm to 900 nm. The dielectric function spectrum of the dense amorphous Al_2O_3 was described by a transparent Cauchy dispersion, with the following form $n(\lambda) = N_0 + N_1/\lambda^2 + N_2/\lambda^4$, where the coefficients N_0, N_1 and N_2 are fitted and restricted to positive values. An effective medium approximation (EMA) was used to model the stack and to fit the measured dielectric function spectra in order to determine the thickness and porosity of the film, which are independent of the wavelength, as prescribed by Aspnes [24]. A rough layer, considered as a homogeneous mixture between the dense Al_2O_3 and air, with 50:50 ratio, was also included as a discrete layer in the model to evaluate the roughness of the film. The thickness value was confirmed by Scanning Electron Microscopy (SEM) analyses of cross sections.

TEM has been used to characterize the effect of the deposition pressure on the microstructure in cross-sectional thin foils prepared by Focused Ions Beam (FIB). The microstructure was then investigated using high angle annular dark field scanning TEM

(HAADF-STEM) in a FEI Titan 80–300 "cubed" TEM, operated at 200 kV and equipped with probe and image aberration correctors. The HAADF-STEM images were acquired using a convergence semi-angle α of 22 mrad and 25 pA probe current. High resolution HAADF-STEM was adopted instead of High Resolution TEM (HRTEM) because of its high sensitivity to slight variations in sample thickness due, for instance, to very small pores. Furthermore, the use of this technique avoids fast electron beam induced crystallization and increase of the pores size as observed during HRTEM imaging. The reduced density functions (RDF), which provide information about the distribution of interatomic distances, have been calculated from selected area electron diffraction (SAED) patterns using the profile analysis of SAD (PASAD) software [25].

2.2. Mechanical testing

2.2.1. Nanoindentation

Nanoindentation measurements were performed using a Berkovich-shape diamond tip, mounted on an Agilent G200 Nanoindenter DCM II head, see Fig. 1.b. The tip area function was calibrated before each measurement, using a fused silica reference. The radius of curvature of the tip end cap was found equal to 55 nm. Standard nanoindentation measurements were performed with an indentation loading rate $\dot{P}/P$ equal to 0.05 s^{-1} (where P is the applied load) at room temperature, with a maximum allowable thermal drift rate limited to 0.05 $nm.s^{-1}$. The indents were performed using the continuous stiffness measurement mode (CSM). The Young's modulus and hardness were calculated using the standard Oliver and Pharr method [26]. Additionally, the Si (100) substrate contribution was subtracted using the method of Hay et al. [27]. Moreover, indentations at loading rates set to 0.05, 0.025, 0.01, 0.005, 0.0025 and 0.0012 s^{-1} were performed in order to determine the strain rate sensitivity (SRS) coefficient m. The lowest indentation strain rates do not allow

reliable depth measurements due to the thermal drift. Hence a correction was applied to samples indented at a non-standard loading rate, based on the hypothesis of rate independent elasticity. The method used is similar to the method suggested by Liu et al. [28], using a fixed reference value of the Young's modulus to recalculate the penetration depth. However, we increased the accuracy of the correction made by Liu et al., by using as reference modulus for each indentation depth, the corresponding Young's modulus obtained at the standard loading rate at the same indentation depth, i.e. the depth h is the solution of the following implicit equation:

$$A_c\left(h-\varepsilon\frac{P}{S}\right)=\frac{4\beta^2}{\pi}\frac{S^2}{E_r^*(h)}$$

where $A_c(h_c)$ is the calibrated area function, S the measured contact stiffness and $E_r^*(h)$ is the reduced modulus at a given depth measured at the standard strain rate of 0.05 s^{-1}. The SRS coefficient (m) is defined as $m = \partial \ln H / \partial \ln \dot{\varepsilon}$ where $\dot{\varepsilon}$ is the indentation strain rate approximately equal to half of the load rate ($\dot{\varepsilon} \approx \dot{P}/2P$) [29]. Here, m was obtained by linear interpolation of the variation of $\ln H$ with $\ln \dot{\varepsilon}$. The corresponding activation volume (V_{act}) for each film was estimated from the strain rate sensitivity and hardness measurements, using the method proposed by Pan et al. [29]:

$$V_{act} = \frac{3\sqrt{3}kT}{mH}, \quad (2)$$

where k is the Boltzmann constant and T the temperature (K).

As explained later when presenting the results in section 3.2, all the characteristic values that will be used as representative of the Al_2O_3 film behavior, i.e. E, H, m and V_{act} were taken from the indentation results obtained at a depth equal to 10% of the thickness. This is the best compromise to minimize both substrate effect and tip rounding effect.

2.2.2. On-chip tensile testing method

The principles of the on-chip uniaxial tensile testing method, shown in Fig. 1.c, have been described in detail elsewhere [22, 23, 30]. The underlying concept is to use the relaxation of the internal stress inside a first material beam to act as a spring-like actuator to induce a pulling force on a test specimen attached to it. The technique enables a large number of tests to be performed with no need of external actuation while avoiding the manipulation of samples and avoiding the measurement of very small loads by any external device. The alignment is also very good, ensuring pure uniaxial tension conditions.

The fabrication of the test device involves several steps. A sacrificial layer is deposited first, here a 2±0.2 μm spin-coated polyimide 2611 from HD MicroSystems, with prior spin-coating of the VM652 adhesion promoter [31]. A PECVD silicon nitride layer is deposited next at 300°C, under a pressure equal to 1.5 mTorr and a power equal to 60 W, with a gas mixture made of SiH_4 (5%) 500 SCCM, NH_3 35 SCCM and N_2 665 SCCM. After lithography, the nitride is etched in a SF_6 plasma in order to obtain the desired actuator beam shapes. The Al_2O_3 layer is deposited by RMS (section 2.1) and patterned with a beam shape using a lift-off resin, deposited prior to the Al_2O_3 layer and removed afterwards. Finally, the etching of the sacrificial layer was performed by oxygen plasma until all structures of interest are released and the sample are deformed until load equilibrium is attained between the actuator and Al_2O_3 beams, see Fig. 1.c. After release, the displacement imposed to the Al_2O_3 beam is measured by SEM. The stress and strain in the specimen are calculated from the measured displacement (u) and from the elastic strain resulting from the presence of a mismatch strain in the actuator (ε_a^{mis}) and in the Al_2O_3 (ε_{ox}^{mis}) beams as:

$$\sigma = E_a \left(\ln\left(\frac{L_{0a}-u}{L_{0a}}\right) - \varepsilon_a^{mis} \right) \frac{S_a}{S}, \quad (3)$$

$$\varepsilon = \ln\left(\frac{L_0+u}{L_0}\right) - \varepsilon_{ox}^{mis}, \quad (4)$$

where E_a is the Young's modulus of the actuator, $L_{0a}$and L_0 are the initial actuator and Al_2O_3 beam lengths, S_a and S are the cross-sectional areas of the actuator and Al_2O_3 beam, respectively. More details concerning the precise extraction of the stress and strain from the displacement can be found in [23]. The complete stress-strain curve can be obtained by testing samples with many different lengths. Note that the determination of the internal stress in the Al_2O_3 is important also for the precise quantification of the mismatch strain in the Al_2O_3 beams (ε_{ox}^{mis}). Moreover, the first deformation point in the stress-strain curve depends on the level of internal stress in the test beam. The lower the internal tensile stress, the smaller the first measured deformation. In the case of large tensile internal stress, one can thus miss the beginning of the curve [12].

3. Results

3.1. Internal stress and microstructure

Fig. 2 shows the evolution of the stress*thickness product as a function of thickness, measured in-situ during reactive cathodic pulverization of Al_2O_3. The internal stress is slightly negative (compressive) at the lowest sputtering pressure, and increases with deposition pressure, becoming positive (tensile) and equal to 353 MPa at 6 mTorr. Above this transition pressure, the internal stress decreases down to 50 MPa at 8 mTorr. The variation of the stress*thickness with respect to thickness is very close to linear in Fig. 2, indicating that there is no significant stress gradient in the films.

The thickness, porosity, roughness and refractive index of the films, extracted by ellipsometry, are listed in Table 1, together with the $< \sigma_f >$ values extracted earlier. The films are assumed to follow a Cauchy dispersion law of the refractive index (n_f) with the wavelength (λ). The refractive index, evaluated at λ=656 nm, is given both for the porous film (n_f) and for the dense part of the film (n_d). The porosity steadily increases from 10.6% to

22.9% when deposition pressure changes from 1.2 mTorr to 8 mTorr, respectively. The roughness slightly increases from 0.7% to 3.1% when pressure increases from 1.2 mTorr to 6 mTorr, and then suddenly rises to 12.4% for the film deposited at 8 mTorr. The refractive index for the porous film (n_f) decreases when pressure increases from 1.2 Torr to 8 mTorr, while the value for the dense part of the film (n_d) remains statistically constant, with an average value equal to 1.739 ± 0.005.

Fig. 3.a, 3.c and 3.d exhibit cross-sectional HAADF-STEM images obtained from the Al_2O_3 films sputtered at 1.2 mTorr, 4 mTorr and 8 mTorr, respectively (see Table 1). The electron diffraction patterns given as insets in all these figures show a halo pattern indicating the amorphous character of the Al_2O_3 microstructure. Note the presence of symmetrical diffraction spots in the diffraction pattern of Fig. 3.d. In this case, because of the small thickness of the Al_2O_3 film, the smallest SAED aperture (~ 200 nm) partially covered the silicon substrate. A homogenous microstructure with no detectable porosity can be observed in Fig. 3.a (1.2 mTorr), and has been confirmed at the nanoscale as seen from the high resolution HAADF-STEM image of Fig. 3.b. In Fig. 3.c the HAADF-STEM image obtained in the film sputtered at 4 mTorr reveals spherical pores with diameter ranging from 2 nm to 12 nm. It is worth noting that pores with diameter around 2 nm (white arrowheads in Fig. 3.c) can hardly be detected because of the very small pore-size/foil-thickness ratio. Thus, the presence of nanosized pores with dimensions less than 1 nm cannot be totally excluded in all films, including the film sputtered at 1.2 mTorr (Fig. 3.a and 3.b). In Fig. 3.c, the film sputtered at 8 mTorr exhibits pores with size ranging from 5 nm to 30 nm.

Fig. 4 shows a comparison between the reduced density functions (RDFs) obtained by quantitative analysis of the SAED patterns from Al_2O_3 films sputtered at 1.7 mTorr, 4 mTorr and 6 mTorr. The positions of the peaks indicated by black arrows are around 1.8 Å, 2.8 Å

and 3.1 Å, in good agreement with the values reported in the literature for the Al-O, O-O and Al-Al bonds, respectively [32, 33, 34]. However, the intensities and positions of the peaks are almost the same for all the RDFs indicating that increasing the deposition pressure (and thus also the porosity) did not substantially affect the RDFs.

3.2. Elastic and viscoplastic properties

Fig. 5.a shows the load versus indentation depth curves, at the standard load rate of 0.05 s^{-1}, for an Al_2O_3 film deposited at 4 mTorr. The responses are highly reproducible. The use of the CSM mode during indentation provides the variations of the Young's modulus (*E*), before and after subtraction of the substrate effect, and of the hardness (*H*) as a function of the indentation depth for films deposited at 1.7 mTorr, 4 mTorr and 6 mTorr (see Fig. 5.b, 5.c and 5.d). The variation of the Young's modulus and of the hardness of the films measured as a function of the deposition pressure, taken as the average value between 9.5% and 10.5% of the thickness, are given in Fig. 5.e and 5.f. This depth is equal to 11 nm, 11.5 nm, 15.6nm, 17.5 nm and 17.7 nm for the 1.2, 1.7, 4, 6 and 8 mTorr film thickness respectively. These depths just meet the 0.2*R* minimum depth criterion, with *R* the radius of the spherical end cap of the diamond indenter, proposed by Chudoba [35] to avoid tip blunting effects. Note that the origin of the small steps at ~130 nm depth in the load versus indentation depth curves of 4 mTorr condition (see Fig. 5.a) has not been identified. These steps do not affect further analysis as all relevant information is extracted at lower indentation depths.

The strain rate sensitivity extracted by nanoindentation is given for films with thicknesses between 740 and 774 nm in Fig. 6.a, as a function of deposition pressure. Fig. 6.b provides the corresponding physical activation volume for each film, computed from the strain rate sensitivity and hardness measurements. The physical activation volume corresponds to the activation volume, defined in equation (2), divided by the transformation

strain associated to the local atomistic shuffling mechanism that was set here equal to 0.1, see Argon [36].

Fig. 7 shows the stress-strain curves obtained from the on-chip microtensile tests for RMS films deposited at 1.7 mTorr and 4 mTorr. No results have been obtained on films deposited at 6mTorr because selfcracking of the film occurs once the sacrificial layer is etched and the film becomes freestanding. The Young's modulus is equal to 209 ± 21 GPa and 127 ± 1 GPa for the 1.7 mTorr and 4 mTorr, respectively.

4. Discussion

4.1. Effect of deposition pressure on internal stress, porosity and roughness

There are three other ways of evaluating the porosity, in addition to the one based on a direct ellipsometric measurement as presented in section 2.1. Two methods use the following formula derived from the Lorentz-Lorenz equation [37] to calculate the pore volume fraction f from the refractive index measurement:

$$f = 1 - \frac{(n_f^2-1)(n_b^2+2)}{(n_f^2+2)(n_b^2-1)}, \tag{5}$$

where n_f is the refractive index of the film given in Table 1 and n_b is the refractive index of the dense part of the film. The value of n_b is then either assumed to be equal to n_d, measured by ellipsometry (see Table 1), or it is assumed to be equal to the refractive index of bulk sapphire (1.77) which constitutes the upper bound for the accessible values of n_b. In both cases, the refractive index of the dense part n_b does not vary significantly with deposition pressure. The last method to evaluate the porosity is explained in section 4.2, and the value of n_b is obtained from model optimization. The low discrepancy, less than 0.04, between the results obtained with the four methods confirms the robustness of the evolution of porosity with deposition pressure, discussed later in this section. The observation of pores by

HAADF-STEM (see Fig. 3.c and 3.d) confirms that part of the porosity is located in these visible pores. However, the HAADF-STEM results do not allow a quantitative determination of the fraction of the porosity associated with these pores.

The roughness increases with pressure, gradually between 1.2 mTorr and 6 mTorr and then with an abrupt increase between 6 mTorr and 8 mTorr (see Fig. 8). The pressure between 6 mTorr and 8 mTorr most presumably corresponds to a critical transition pressure, called "thermalization pressure" (P_c) [38], under which the particles travel ballistically through the plasma and attain the growing surface with high velocity. Increasing the pressure also increases the number of collisions in the plasma, decreasing the kinetic energy of the species. Above P_c, particles attain the substrate with an energy reduced to the thermal energy. Zhou et al. [38] combined the thermalization effect to a model of aggregate formation to explain the abrupt roughness transition observed above P_c. In their model, above P_c, the size of the clusters increases with pressure. The same model explains the observed jump in roughness between 6 mTorr and 8 mTorr. The gradual increase of roughness under P_c, where we assume there is no cluster aggregation, is attributed to the decreasing particle impact smoothing effect with increasing pressure, due to the decreasing kinetic energy of the species.

This process of formation of aggregates (above P_c), combined to the decrease of the energy of the species when hitting the substrate (under P_c), contributes to increasing the porosity. Below P_c, the porosity increase probably originates, as roughness does, from the decreasing particle impact smoothing effect with pressure. Above P_c, the porosity increase is related to the larger residual pores after sintering of the largest aggregates [38]. These hypotheses agree with the measured increase of porosity with pressure, see also Fig. 8.

The internal stress in the films depends on the deposition pressure as well. The film deposited at 1.2 mTorr involves a small compressive internal stress, with no transition due to

Volmer-Weber growth mode observed (within the resolution limits). The Volmer-Weber mode is indeed associated with variations of the measured internal stresses along deposition, due to the formation of initial 3D islands, which grow on the substrate and subsequently coalesce to form a continuous film [39]. The compressive stress at low gas pressure is due to "atomic peening", when the species attain the surface with a high kinetic energy after their ballistic travel through the plasma [38]. The films deposited at 1.7 mTorr, 4 mTorr and 6 mTorr all exhibit the same trend in Fig. 2, with final tensile stress increasing with deposition pressure. These three conditions involve an almost constant tensile stress up to the end of deposition. Mayr et al. [40] observed the same tensile regime in amorphous $Zr_{65}Al_{7.5}Cu_{27.5}$, with an additional slightly compressive stress during the first nanometers of growth, which could not be observed in this case (within the resolution limit). They associated again this initial compressive regime to "atomic peening". Due to the increasing film roughness and porosity with increasing deposition pressure (under P_c), kinetic-induced growth instabilities (self-shadowing) also increase with increasing deposition pressure. Mayr et al. [40] called the subsequent energy minimization process that generates the late stage tensile regime and that involves atomic dynamic, the « continuous viscous coalescence mechanism of the clusterlike film ». By increasing the deposition pressure from 1.7 mTorr to 6 mTorr, the clusterlike film viscous coalescence process dominates, leading to a larger tensile stress. The film deposited at 8 mTorr has a low level of tensile internal stress, all along the deposition process. This lower stress is believed to arise from the in-situ sintering of the aggregates forming the growing film above P_c, as suggested by Zhou et al. [38]. These conditions involve no "atomic peening", since the species only attain the substrate with thermal kinetic energy and after they formed clusters. Note finally that the high levels of internal stress can cause severe mechanical reliability issues in applications, such as buckling or fracture [39]. It is therefore essential to determine which deposition conditions can minimize the level of internal stress.

1
2
3
4
5
6
7
8
9
10
11
12
13
14
15
16
17
18
19
20
21
22
23
24
25
26
27
28
29
30
31
32
33
34
35
36
37
38
39
40
41
42
43
44
45
46
47
48
49
50
51
52
53
54
55
56
57
58
59
60
61
62
63
64
65

4.2. Effect of microstructure on elastic properties

The Young's modulus *E* of the films, obtained with the on-chip microtensile tests, see Fig. 7, agrees with the nanoindentation data (Fig. 5.e). This agreement also confirms the absence of any significant elastic anisotropy, considering that the main loading direction is different in these two loading configurations. The magnitude of the Young's modulus is significantly lower than in α-alumina, which varies between 350-390 GPa [41] and 500 GPa [1, 42], depending on the studies. The value for the films deposited at 1.7 mTorr, equal to 179 ± 5 GPa (from nanoindentation), is in good agreement with the values reported by Koski et al. equal to 206 GPa and 182 GPa for amorphous alumina deposited by RMS at 2.3 mTorr and 7.7 mTorr, respectively [16].

The self-cracking issue encountered with the lab-on-chip sample for the film deposited at 6 mTorr originates from the high internal stress (see Fig. 2), which is presumably higher than the fracture stress of the film. Note that, since self-fracture occurs only when the film is liberated from the substrate, the 6 mTorr films could be analyzed by nanoindentation to extract Young's modulus, hardness and strain rate sensitivity.

The overall elastic modulus decreases with increasing deposition pressure and therefore with increasing porosity, as is expected. The measured Young's modulus is a homogenized quantity and not the true elastic stiffness of the alumina matrix material around the pores. In order to extract the true Young's modulus of Al_2O_3 and to separate it from the impact of the porosity, the predictions given by the Mori-Tanaka model [43, 44] for porous materials with spherical voids are compared to the experimental evolution of the Young's modulus with porosity, measured by nanoindentation and by on-chip testing (Fig. 9). The Mori-Tanaka model assumes that each pore behaves as if it was surrounded by an infinite solid made of the matrix material, with the strain at infinity being the average strain in the

1
2
3
4
5
6
7
8
9
10
11
12
13
14
15
16
17
18
19
20
21
22
23
24
25
26
27
28
29
30
31
32
33
34
35
36
37
38
39
40
41
42
43
44
45
46
47
48
49
50
51
52
53
54
55
56
57
58
59
60
61
62
63
64
65

matrix constituent of the composite. The result, based on Eshelby's solution, coincides with the Hashin-Shtrikman upper bound in the present case of spherical pores [44]. As mentioned in section 4.1, the porosity is evaluated by using the Lorentz-Lorenz equation, using the refractive index n_f measured by ellipsometry and assuming that the refractive index of the dense amorphous part n_b is unknown. This parameter was then fitted for each series of points, together with the unknown Young's modulus, to follow at best the model predictions. The idea is to determine if the presence of porosity is the only reason for the decrease of the overall Young's modulus. Other homogenization models involving ellipsoidal shapes were also attempted but led to qualitatively similar variations of Young's modulus, always significantly smaller than the experimental variation. As explained above, the similar evolution of the Young's modulus with both on-chip testing and nanoindentation, whereas these methods induce different principal loading directions, confirms the absence of significant anisotropy in the porosity distribution that could explain the observed mechanical response. This is confirmed also by the spherical shape of the pores observed by HAADF-STEM (see Fig. 3.c and 3.d).

The most obvious explanation for the large drop in elastic stiffness is that the Young's modulus of the dense part is not constant but evolves with deposition pressure as well. Our best estimates, based on the Mori-Tanaka model, for the "intrinsic" E_0 for the five alumina films analyzed by nanoindentation and for the two alumina films analyzed with the on-chip testing are given in Table 2. The results, for both types of measurements, indicate that increasing the deposition pressure also decreases the intrinsic Young's modulus of the non-porous amorphous alumina. The decrease of the intrinsic modulus could be due to a change in the amorphous alumina at the atomic level, involving a more open and more flexible atomic arrangement. However, no confirmation of this assumption could be brought by the comparison of the SAED patterns, as all the obtained RDFs exhibit the same positions and

1
2
3
4
5
6
7
8
9
10
11
12
13
14
15
16
17
18
19
20
21
22
23
24
25
26
27
28
29
30
31
32
33
34
35
36
37
38
39
40
41
42
43
44
45
46
47
48
49
50
51
52
53
54
55
56
57
58
59
60
61
62
63
64
65

intensities of the peaks (see section 3.1). This confirms the observation of Tane et al. [33] who have shown that the porosity, elastic stiffness and density of annealed amorphous Al_2O_3 thin films prepared by electron beam deposition increase with annealing time while the RDFs remain the same as they were before annealing. Using molecular dynamics simulations, the authors attributed such a feature to the inhomogeneity of density in the as-deposited films with the presence of unstable low-density regions containing a low fraction of stable AlO_6 units and stable high-density regions containing a high fraction of stable AlO_6 units [33].

4.3. Effect of microstructure on hardness and viscoplastic response

All on-chip test specimens fail in a brittle manner before plastic yielding, and this despite the small size of the samples. The fracture stress decreases with increasing porosity as expected (see Fig. 7). The statistical analysis of the fracture behavior requires more data and is left for future investigations.

The nanoindentation hardness H is significantly lower than the 30 GPa obtained for α-alumina [42]. The hardness of films deposited at 1.7 mTorr, equal to 12.3 ± 0.5 GPa, is in the range of values reported by Koski et al. equal to 20.6 GPa and to 12.6 GPa for amorphous alumina deposited by RMS at 2.3 mTorr and 7.7 mTorr, respectively [16]. The overall hardness decreases with porosity in a way similar to the Young's modulus. The overall strain ε_Y, corresponding to the overall elastic limit σ_Y, and given by

$$\varepsilon_Y = \frac{\sigma_Y}{E} \approx \frac{H}{2{,}8\,E} \quad (6)$$

shows however a slight decreasing trend (see Table 3). Note that this formula assumes that the hardness is equal to 2.8 times the elastic limit as for metallic polycrystals with no strain hardening. The factor 2.8 must be considered with caution because it is an upper bound for materials with low E/σ_Y ratio [45, 46]. The ε_Y, between 0.018 and 0.025 are slightly lower than 0.027, the theoretical value for many amorphous materials, and close to the value 0.022

obtained by Nayar et al. [47] for amorphous alumina thin films deposited by e-beam evaporation.

The calculated σ_Y is a homogenized quantity and not the true yield stress of the alumina matrix material. In order to extract the yield stress of Al_2O_3 and to separate it from the impact of porosity, the predictions by Fleck et al. [48] with a Gurson type model for porous materials are compared to the experimental evolution of the hardness with porosity measured by nanoindentation. Our best estimates for the "intrinsic" σ_{Y0} and $\varepsilon_{Y0} = \frac{\sigma_{Y0}}{E_0}$ for the five alumina films analyzed by nanoindentation, based on the Gurson model, are given in Table 3. Both the overall and intrinsic yield stress decrease with porosity, but the decrease is less pronounced for σ_{Y0}. This decrease with increasing deposition pressure can be the result of a more open atomic structure. The intrinsic strain corresponding to the elastic limit ε_{Y0} is slightly higher than the overall value (see Fig. 10). The ε_{Y0} do not vary with deposition pressure, resulting in an average of 0.025 ± 0.002, in statistical agreement with the theoretical 0.027 reference. This brings additional confidence in the validity of the overall procedure used to extract E_0 and σ_{Y0}.

Regarding the viscoplastic response, the analysis of strain rate sensitivity of amorphous materials has been subject of different studies, in particular for bulk metallic glasses [49], but also for covalent, metallic, ionic and superionic glasses [50]. The Al_2O_3 films show a moderate strain rate sensitivity m ~ 0.016, statistically independent of porosity (see Fig. 6.a). This is in the range of the strain rate sensitivities measured for soda lime silicates and other ionic glasses [50]. The strain rate sensitivity is indeed believed to be insensitive to porosity below a threshold level, as demonstrated by Limbach et al. [50], who could not detect any significant influence of the atomic packing density on the strain rate sensitivity for moderates to high packing degree. Fig. 6.b shows the increase of the physical

activation volume with deposition pressure, which confirms the hypothesis of a weaker atomic arrangement of the Al_2O_3 clusters in the amorphous structure, as already inferred from the elastic properties. The values correspond to around 10 to 25 atomic Al_2O_3 clusters, which has a typical dimension of the order of 100 A^3.

5. Conclusions

The porosity and the roughness of amorphous Al_2O_3 films as well as the internal stress were modified by changing the deposition pressure during RMS sputtering. The dependence of the mechanical properties of Al_2O_3 layers on the film microstructure has been investigated. The main conclusions of the study are the following.

- The porosity of the film steadily increases with deposition pressure, as a result of a combination of different phenomena. A transition from atomic peening into the surface to aggregate formation in the gas phase occurs when the pressure exceeds the thermalization pressure, leading to a transition in roughness amplitude. Atomic peening is also responsible for the compressive internal stresses in the film deposited at low pressure. All other films exhibit tensile internal stress, which increases with increasing deposition pressure, up to a maximum for films deposited at the thermalization pressure, to finally decrease for the film deposited at the highest pressure.
- The overall Young's modulus decreases with increasing pressure. Homogenization models showed that this decrease is not only attributed to the porosity, but must be also related to variations in the intrinsic amorphous Al_2O_3 arrangement. Increasing the deposition pressure could lead to a more open amorphous structure. The similar evolution of the overall Young's modulus in both on-chip testing and nanoindentation test methods confirms that there is no strong elastic anisotropy. Furthermore, the 2 to 30 nm sized pores observed by using HAADF-STEM exhibit spherical shapes.

- The similar evolution of the overall Young's modulus and overall hardness with porosity is such that the strain ε_Y, corresponding to the overall elastic limit σ_Y, shows only a slight evolution with porosity. The intrinsic strain ε_{Y0}, corresponding to the intrinsic elastic limit σ_{Y0} of the material surrounding the pores, shows no significant evolution with porosity and was found to be statistically equal to the theoretical value of 0.027 for amorphous solids. This is also an indication that the elastic and plastic mechanisms are both related to the same atomistic phenomena.
- The strain rate sensitivity of amorphous alumina thin films deposited by RMS was found equal to 0.016, similar to those of soda lime silicates, with no significant influence of the porosity. Due to the decrease of hardness with porosity, the corresponding physical activation volume increases with porosity, further confirming the change in amorphous Al_2O_3 atomic arrangement.

Further work will study the effect of deposition conditions on the fracture stress. This will be achieved by statistical analysis of the fracture strain of on-chip testing samples, by taking advantage of the large number of samples that can be produced simultaneously using that technique. The impact of the surface native oxide layer on the elastic and plastic behavior of metallic layers will also be addressed in future studies.

1
2
3
4
5
6
7
8
9
10
11
12
13
14
15
16
17
18
19
20
21
22
23
24
25
26
27
28
29
30
31
32
33
34
35
36
37
38
39
40
41
42
43
44
45
46
47
48
49
50
51
52
53
54
55
56
57
58
59
60
61
62
63
64
65

Acknowledgments

This work has been funded by the Belgian Science Policy through the IAP 7/21 project. The support of the 'Fonds Belge pour la Recherche dans l'Industrie et l'Agriculture (FRIA)' for A.v.d.R. is also gratefully acknowledged, as well as the support of FNRS through the grant PDR T.0122.13 "Mecano".

References

[1] C. Cibert, H. Hidalgo, C. Champeaux, P. Tristant, C. Tixier, J. Desmaison, A. Catherinot, Properties of aluminum oxide thin films deposited by pulsed laser deposition and plasma enhanced chemical vapor deposition, Thin Solid Films 516 (2008) 1290-1296

[2] C.H. Lin, H.L. Wang, M.H. Hon, The effect of residual stress on the adhesion of PECVD-coated aluminum oxide film on glass, Thin Solid Films 283 (1996) 171-174

[3] Y.S. Chaug, N. Roy, Thin Solid Films 193-194 (1990) 959-964

[4] R. Kotipalli, R. Delamare, O. Poncelet, X. Tang, L.A. Francis, D. Flandre, Passivation effects of atomic-layer-deposited aluminum oxide, EPJ Photovoltaics 4 (2013) 45107

[5] W. Lee, The anodization of aluminum for nanotechnology applications, JOM 62(6) (2010) 57-63

[6] A. Mozalev, R. Calavia, R.M. Vazquez, I. Gracia, C. Cane, X. Correig, X. Vilanova, F. Gispert-Guirado, J. Hubalek, E. Llobet, MEMS-microhotplate-based hydrogen gas sensor utilizing the nanostructured porous-anodic-alumina-supported WO_3 active layer, Int. J. Hydrogen Energy 38 (2013) 8011-8021

[7] B. Bhushan, "Nanowires", in: Springer Handbook of Nanotechnology, eds.: Springer Verlag Berlin Heidelberg, 2004. pp. 99-138

[8] E.K. Baumert, O.N. Pierron, Fatigue properties of atomic-layer-deposited alumina ultra-barriers and their implications for the reliability of flexible organic electronics, Appl. Phys. Lett. 101 (2012) 251901

[9] J. Moghal, H. Suttle, A. Cook, C. Grovenor, H. Assender, Investigation of the mechanical properties of aluminium oxide thin films on polymer substrates by a combination of fragmentation and scratch testing, Surf. Coat. Technol. 206 (2012) 3309-3315

[10] P. C. Snijders, L. P. H. Jeurgens, W. G. Sloof, Structural ordering of ultra-thin, amorphous aluminium-oxide films, Surf. Sci. 496 (2002) 97

[11] M. T. A. Saif, S. Zhang, A. Haque, K.J. Hsia, Effect of Native Oxide on the Elastic Response of Nanoscale Al Films, Acta Mater. 50 (2002) 2779-2786

[12] M. Coulombier, PhD Thesis, Université Catholique de Louvain (Belgique) (2012)

[13] C. Brugger, M. Coulombier, T.J. Massart, J.-P. Raskin, T. Pardoen, Strain gradient plasticity analysis of the strength and ductility of thin metallic films using an enriched interface model, Acta Mater 58 (2010) 4940-4949

[14] F. Diologent, R. Goodall, A. Mortensen, Surface oxide in replicated microcellular aluminium and its influence on the plasticity size effect, Acta Mater. 57 (2009) 286-294

[15] C. Ayas, V.S. Deshpande, M.G.D. Geers, Tensile response of passivated films with climb assisted dislocation glide, J. Mech. Phys. Solids 60(9) (2012) 1626-1643

[16] K. Koski, J. Hölsä, P. Juliet, Deposition of aluminium oxide thin films by reactive magnetron sputtering, Surf. Coat. Technol. 116-119 (1999) 716-720

[17] J. Wang, Y.-H. Yu, S.C. Lee, Y.-W. Chung, Tribological and optical properties of crystalline and amorphous alumina thin films grown by low-temperature reactive magnetron sputter-deposition, Surf. Coat. Technol. 146-147 (2001) 189-194

[18] J. Bauer, A. Schroer, R. Schwaiger, I. Tesari, C. Lange, L. Valdevit, O. Kraft, Push-to-pull tensile testing of ultra-strong nanoscale ceramic–polymer composites made by additive manufacturing, Extrem. Mech. Lett. 3 (2015) 105-112

[19] M.G. Mueller, V. Pejchal, G. Zagar, A. Singh, M. Cantoni, A. Mortensen, Fracture toughness testing of nanocrystalline alumina and fused quartz using chevron-notched microbeams, Acta Mater. 86 (2015) 385-395

[20] J. Proost, F. Spaepen, Evolution of the growth stress, stiffness, and microstructure of alumina thin films during vapor deposition, J. Appl. Phys. 91(1) (2002) 204-216

[21] S. Michotte, J. Proost, In situ measurement of the internal stress evolution during sputter deposition of ZnO:Al, Sol. Energ. Mat. Sol. Cells 98 (2012) 253-259

[22] S. Gravier, M. Coulombier, A. Safi, N. André, A. Boe, J.-P. Raskin, T. Pardoen, New On-Chip Nanomechanical Testing Laboratory - Applications to Aluminum and Polysilicon Thin Films, IEEE J. Mirco. Syst. 18 (2009) 555-569

[23] R. Vayrette, J.-P. Raskin, T. Pardoen, On-chip fracture testing of freestanding nanoscale materials, Eng. Fract. Mech., 150 (2015) 222-238

[24] D. Aspnes, Optical properties of thin films, Thin Solid Films 89(3) (1982) 249-262

[25] C. Gammer, C. Mangler, C. Rentenberger, H.P. Karnthaler, Quantitative local profile analysis of nanomaterials by electron diffraction, Scr. Mater. 63 (2010) 312-315

[26] W.C. Oliver, G.M. Pharr, An improved technique for determining hardness and elastic modulus using load and displacement sensing indentation experiments, J. Mater. Res. 7 (1992) 1564-1583

[27] J. Hay, B. Crawford, Measuring substrate-independent modulus of thin films, J. Mater. Res. 26 (2011) 727-738

[28] Y. Liu, J. Hay, H. Wang, X. Zhang, A new method for reliable determination of strain-rate sensitivity of low-dimensional metallic materials by using nanoindentation, Scr. Mater. 77 (2014) 5-8

[29] D. Pan, A. Inoue, T. Sakurai, M.W. Chen, Experimental characterization of shear transformation zones for plastic flow of bulk metallic glasses, Proc. Natl. Acad. Sci. U.S.A. 105 (2008) 14769

[30] M.-S. Colla, B. Amin-Ahmadi, H. Idrissi, L. Malet, S. Godet, J.-P. Raskin, D. Schryvers, T. Pardoen, Dislocation-mediated relaxation in nanograined columnar palladium films revealed by on-chip time-resolved HRTEM testing, Nat. Commun. 6 (2015) 5922

[31] T. Walewyns, N. Reckinger, S. Ryelandt, T. Pardoen, J.-P. Raskin, L. Francis, Polyimide as a versatile enabling material for microsystems fabrication: surface micromachining and electrodeposited nanowires integration, J. Micromech. Microeng. 23 (2013) 095021

[32] P. Lamparter, R. Kniep, Structure of amorphous Al_2O_3, Physica B 234–236 (1997) 405-406

[33] M. Tane, S. Nakano, R. Nakamura , H. Ogi, M. Ishimaru , H. Kimizuka , H. Nakajima, Nanovoid formation by change in amorphous structure through the annealing of amorphous Al_2O_3 thin films, Acta Mater 59 (2011) 4631–4640

[34] S. Davis, G. Gutiérrez, Structural, elastic, vibrational and electronic properties of amorphous Al_2O_3 from *ab initio* calculations, J. Phys.: Condens. Matter 23 (2011) 495401

[35] T. Chudoba, “Chapter 6: Measurement of hardness and Young's modulus of coatings by nanoindentation”, in: Nanostructured coatings, eds.: A. Cavaleiro and J.Th.M. De Hosson, 2006. pp. 216-260

[36] A. Argon, “Inelastic behavior of non-polymeric glasses”, in: The Physics of Deformation and Fracture of Polymers, eds.: Cambridge university press, 2013. pp. 174-227

[37] M. Born, E. Wolf, “The Lorentz-Lorenz formula”, in: Principle of Optics 7th edition, eds.: Cambridge university press, 1999. pp. 93

[38] L. Zhou, Y. Wang, H. Zhou, M. Li, R.L. Headrick, K. MacArthur, B. Shi, R. Conley, A.T. Macrander, Pressure-dependent transition from atoms to nanoparticles in magnetron sputtering: Effect on WSi_2 film roughness and stress, Phys. Rev. B 82 (2010) 075408

[39] J.A. Floro, S.J. Hearne, J.A. Hunter, P. Kotula, E. Chason, S.C. Seel, C.V. Thompson, The dynamic competition between stress generation and relaxation mechanisms during coalescence of Volmer–Weber thin films, J. Appl. Phys. 89(9) (2001) 4886-4897

[40] S.G. Mayr, K. Samwer, Model for Intrinsic Stress Formation in Amorphous Thin Films, Phys. Rev. Lett. 87 (2001) 036105

[41] Z. Xia, L. Riester, B.W. Sheldon, W.A. Curtin, J. Liang, A. Yin, J.M. Xu, Mechanical properties of highly ordered nanoporous anodic alumina membranes, Rev. Adv. Mater. Sci. 6 (2004) 131-139

[42] N.G. Chechenin, J. Bottiger, J.P. Krog, Nanoindentation of amorphous aluminum oxide films I. The influence of the substrate on the plastic properties, Thin Solid Films 261 (1995) 219-227

[43] T. Mori, K. Tanaka, Average stress in matrix and average elastic energy of materials with misfitting inclusions, Acta Metall. 21 (1973) 571-574

[44] M.I. El Ghezal, Y. Maalej, I. Doghri, Micromechanical models for porous and cellular materials in linear elasticity and viscoelasticity, Comput. Mater. Sci., 70 (2013) 51-70

[45] P. Zhang, S.X. Li, Z.F. Zhang, General relationship between strength and hardness, Mater. Sci. Eng. A 529 (2011) 62-73

[46] A. Clausner, F. Richter, Determination of yield stress from nano-indentation experiments, Eur. J. Mech.-A/Solids 51 (2015) 11-20

[47] P. Nayar, A. Khanna, D. Kabiraj, S.R. Abhilash, B.D. Beake, Y. Losset, B. Chen, Structural, optical and mechanical properties of amorphous and crystalline alumina thin films, Thin Solid Films 568 (2014) 19-24

[48] N.A. Fleck, H. Otoyo, A. Needleman, Indentation of porous solids, Int. J. Struct. 29(13) (1992) 1613-1636

[49] M. Ghidelli, S. Gravier, J.-J. Blandin, P. Djemia, F. Monpiou, G. Abadias, J.-P. Raskin, T. Pardoen, Extrinsic mechanical size effects in thin ZrNi metallic glass films, Acta Mater. 90 (2015) 232-241

[50] R. Limbach, B.P. Rodrigues, L. Wondraczek, Strain-rate sensitivity of glasses, J. Non-Cryst. Solids 404 (2012) 124-134

Table captions

Table 1. Average internal stress $< \sigma_f >$ extracted from the substrate curvature change (Fig. 2) and thickness, porosity, roughness and refractive indices n_f, and n_d of the films obtained from ellipsometric measurements.

Table 2. Effective Young's modulus (E) and Young's modulus of the dense part of the films E_0 for each deposition pressure, as computed with the Mori-Tanaka model. The porosities used in the model are the values obtained by ellipsometry (Table 1).

Table 3. Effective yield stress σ_Y and the corresponding strain ε_Y, yield stress σ_{Y0} of the alumina matrix surrounding the pores and corresponding strain ε_{Y0} for each deposition pressure computed from Gurson model, using the indicated "Gurson factor" values. The porosities used in the model are the values obtained by ellipsometry (Table 1) and the Young's modulus values are the ones obtained by nanoindentation (Table 2).

Figure captions

Fig. 1. Schematic illustrations of the mechanical characterization methods used in this study. (a) Multibeam Optical Stress Sensor (MOSS) used to monitor the change of curvature of the substrate and extract the internal stress evolution in the film in-situ during deposition. (b) Nanoindentation using a diamond tip to evaluate the Young's modulus, hardness, and strain rate sensitivity of the films. (c) Elementary on-chip uniaxial tensile test cell before and after the tensile testing, which is activated by the selective etching of the sacrificial layer.

Fig. 2. Internal stress evolution as a function of the deposition pressure *p* (given in mTorr) during reactive magnetron sputtering of amorphous Al_2O_3 thin films. Internal stress values are equal to the slope of the curves, and are globally constant throughout the film, indicating no major internal stress gradients are present. The average internal stress $< \sigma_f >$ is given for each film.

Fig. 3. (a, c, d) HAADF-STEM images and SAED patterns from Al_2O_3 films sputtered at 1.2 mTorr, 4 mTorr and 8 mTorr, respectively. (b) High resolution HAADF-STEM at the Al_2O_3/Silicon interface from (a). Note the difficulty to detect very small pores (~2 nm) as indicated by white arrowheads in (c). In addition to the 'large' pores (~30 nm) shown in (d), smaller pores (~5 nm) were observed as indicated by white arrowheads in the top left inset of the same figure.

Fig. 4. Reduced density function G(r) of amorphous Al_2O_3 films sputtered at 1.7 mTorr, 4 mTorr and 6 mTorr. The peaks are identified by reference to the literature ([32, 33, 34]).

Fig. 5. (a) Variation of the indentation load as function of the displacement into the surface for sixteen indents in the Al_2O_3 thin film deposited at 4 mTorr. (b,c,d) Apparent Young's modulus, Young's modulus computed after subtracting the effect of the substrate and hardness as a function of the indentation depth for Al_2O_3 films deposited at 1.7 mTorr, 4 mTorr and 6 mTorr. (e) Young's modulus and (f) Hardness variation as a function of the deposition pressure for Al_2O_3 films deposited by reactive magnetron sputtering.

Fig. 6. Variation of the strain rate sensitivity coefficient (a) and physical activation volume (b) as a function of the deposition pressure of sputtered Al_2O_3 thin films.

Fig. 7. Stress-strain curves of the Al_2O_3 films deposited at 1.7 mTorr and 4 mTorr, respectively 170 and 220 nm-thick. The Young's modulus is equal to the slope of the linear interpolation.

Fig. 8. Variation of the porosity and roughness as a function of the deposition pressure for Al_2O_3 films deposited by reactive magnetron sputtering. The "thermalization pressure" (P_c) is indicated, corresponding to the abrupt increase in the roughness of the films.

Fig. 9. Variation of the Effective normalized Young's modulus as a function of film porosity. Experimental measurements obtained by nanoindentation and by the on-chip testing method are fitted to the models of Mori-Tanaka in the case of spherical voids [44]. The Voigt model prediction is also indicated.

Fig. 10. Variation of the overall strain ε_Y, corresponding to the effective yield stress σ_Y, and strain ε_{Y0} of the alumina matrix surrounding the pores, corresponding to the yield stress σ_{Y0} computed from Gurson model, as a function of the deposition pressure. The average value of ε_{Y0} is 0.025 ± 0.002. The theoretical value for many amorphous materials of 0.027 is also indicated.

Figure(s)

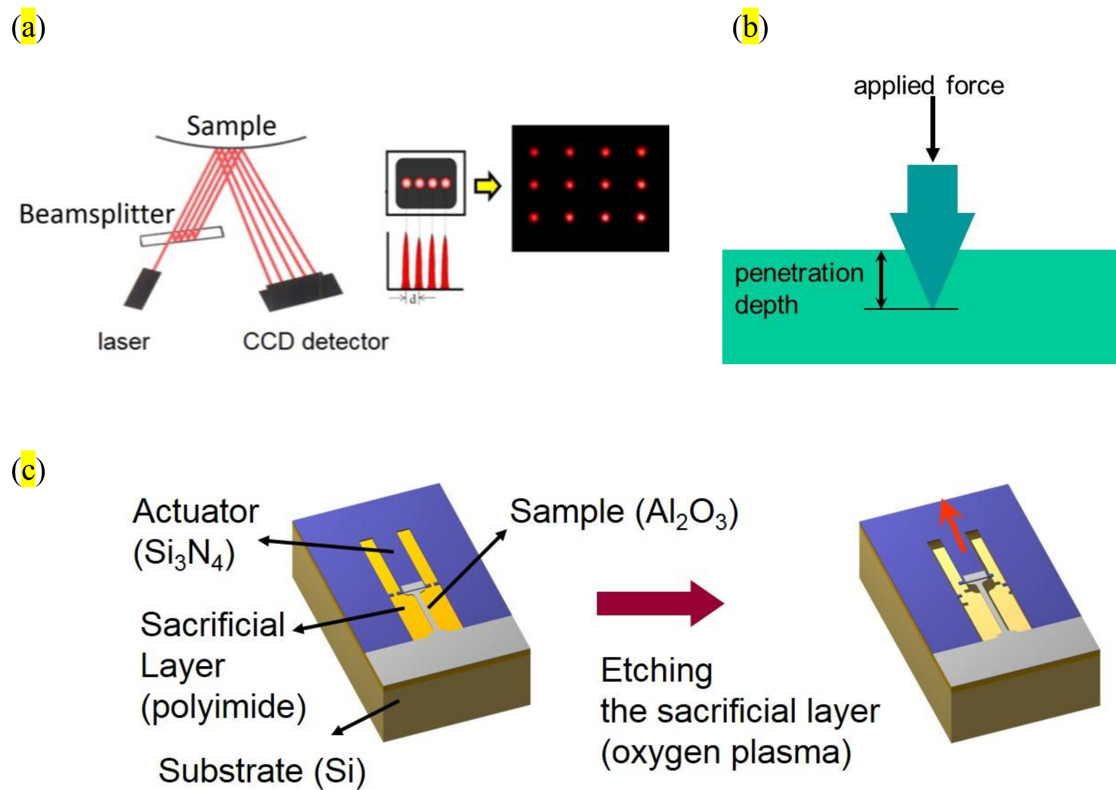

Fig. 1. Schematic illustrations of the mechanical characterization methods used in this study. (a) Multibeam Optical Stress Sensor (MOSS) used to monitor the change of curvature of the substrate and extract the internal stress evolution in the film in-situ during deposition. (b) Nanoindentation using a diamond tip to evaluate the Young's modulus, hardness, and strain rate sensitivity of the films. (c) Elementary on-chip uniaxial tensile test cell before and after the tensile testing, which is activated by the selective etching of the sacrificial layer.

Figure(s)

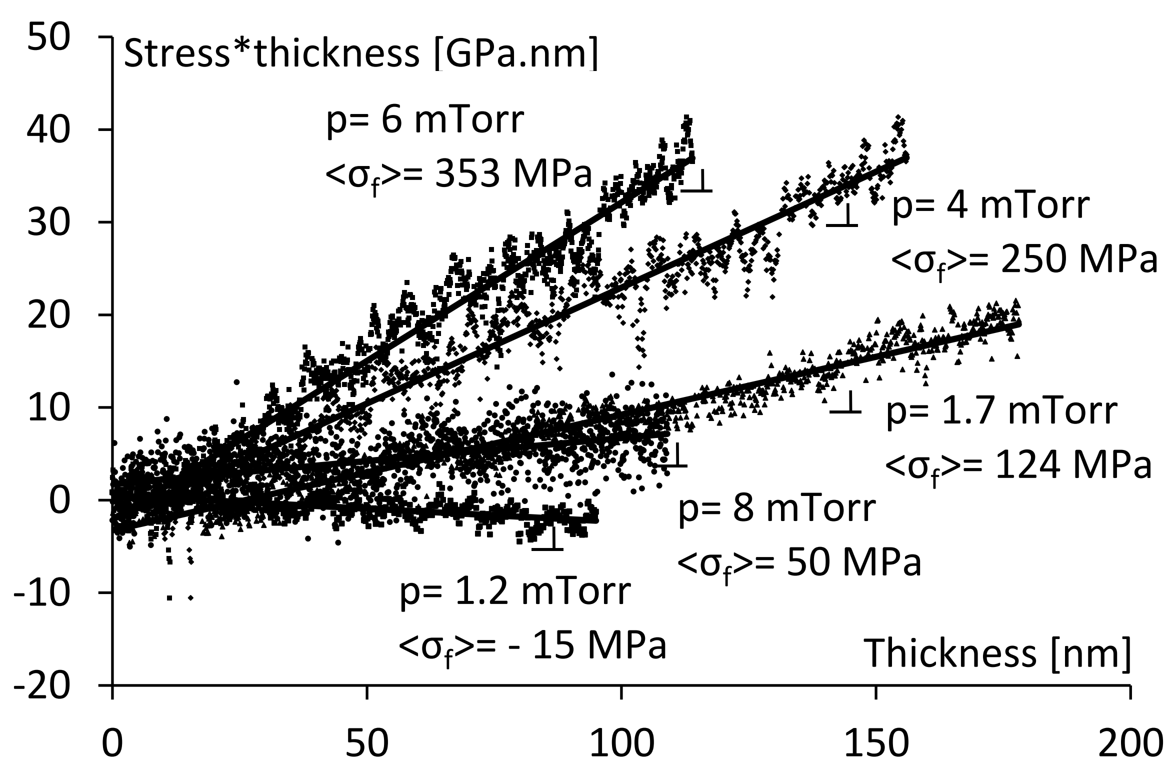

Fig. 2. Internal stress evolution as a function of the deposition pressure p (given in mTorr) during reactive magnetron sputtering of amorphous Al_2O_3 thin films. Internal stress values are equal to the slope of the curves, and are globally constant throughout the film, indicating no major internal stress gradients are present. The average internal stress $< \sigma_f >$ is given for each film.

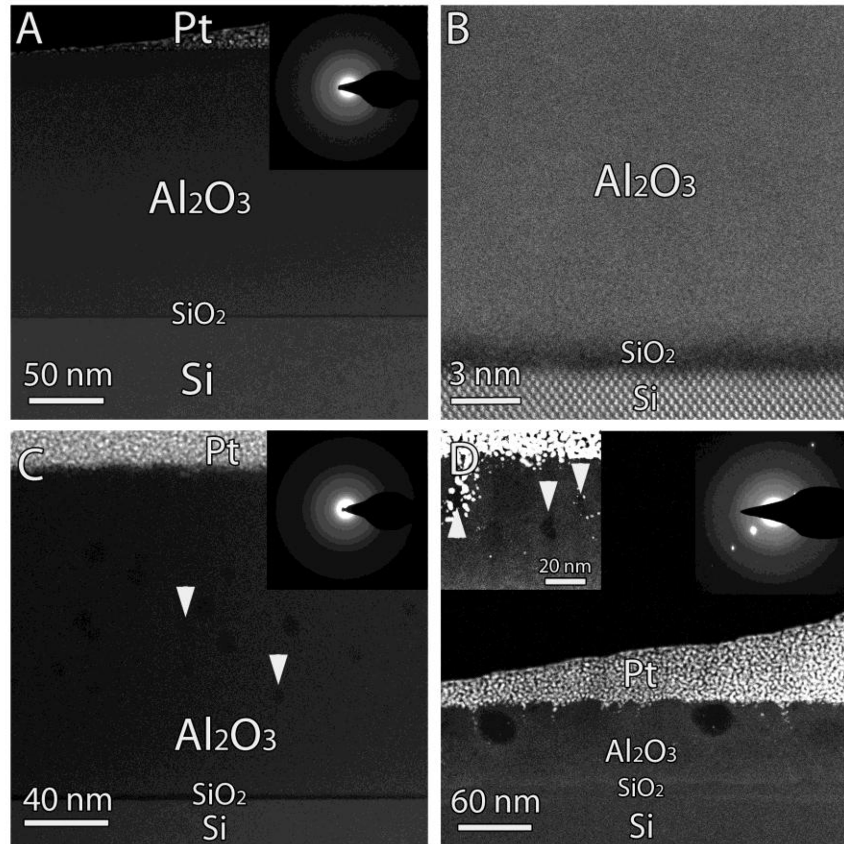

Fig. 3. (a, c, d) HAADF-STEM images and SAED patterns from Al_2O_3 films sputtered at 1.2 mTorr, 4 mTorr and 8 mTorr, respectively. (b) High resolution HAADF-STEM at the Al_2O_3/Silicon interface from (a). Note the difficulty to detect very small pores (~2 nm) as indicated by white arrowheads in (c). In addition to the 'large' pores (~30 nm) shown in (d), smaller pores (~5 nm) were observed as indicated by white arrowheads in the top left inset of the same figure.

Figure(s)

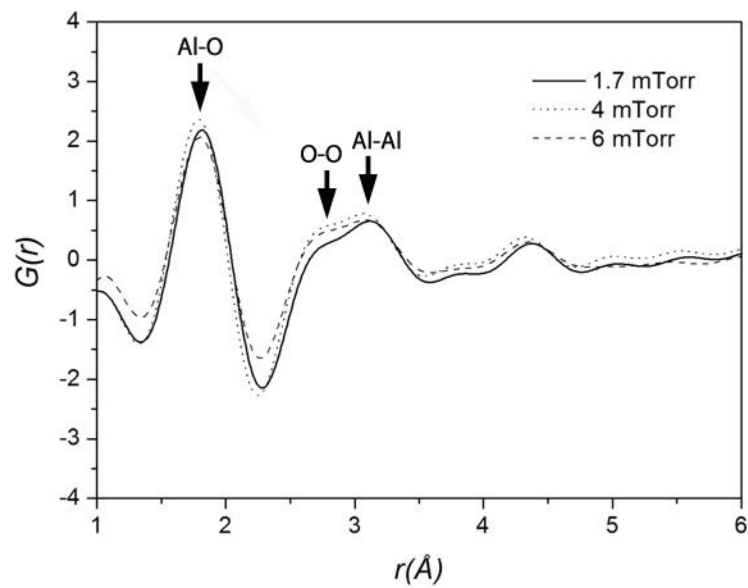

Fig. 4. Reduced density function G(r) of amorphous Al_2O_3 films sputtered at 1.7 mTorr, 4 mTorr and 6 mTorr. The peaks are identified by reference to the literature ([32, 33, 34]).

Figure(s)

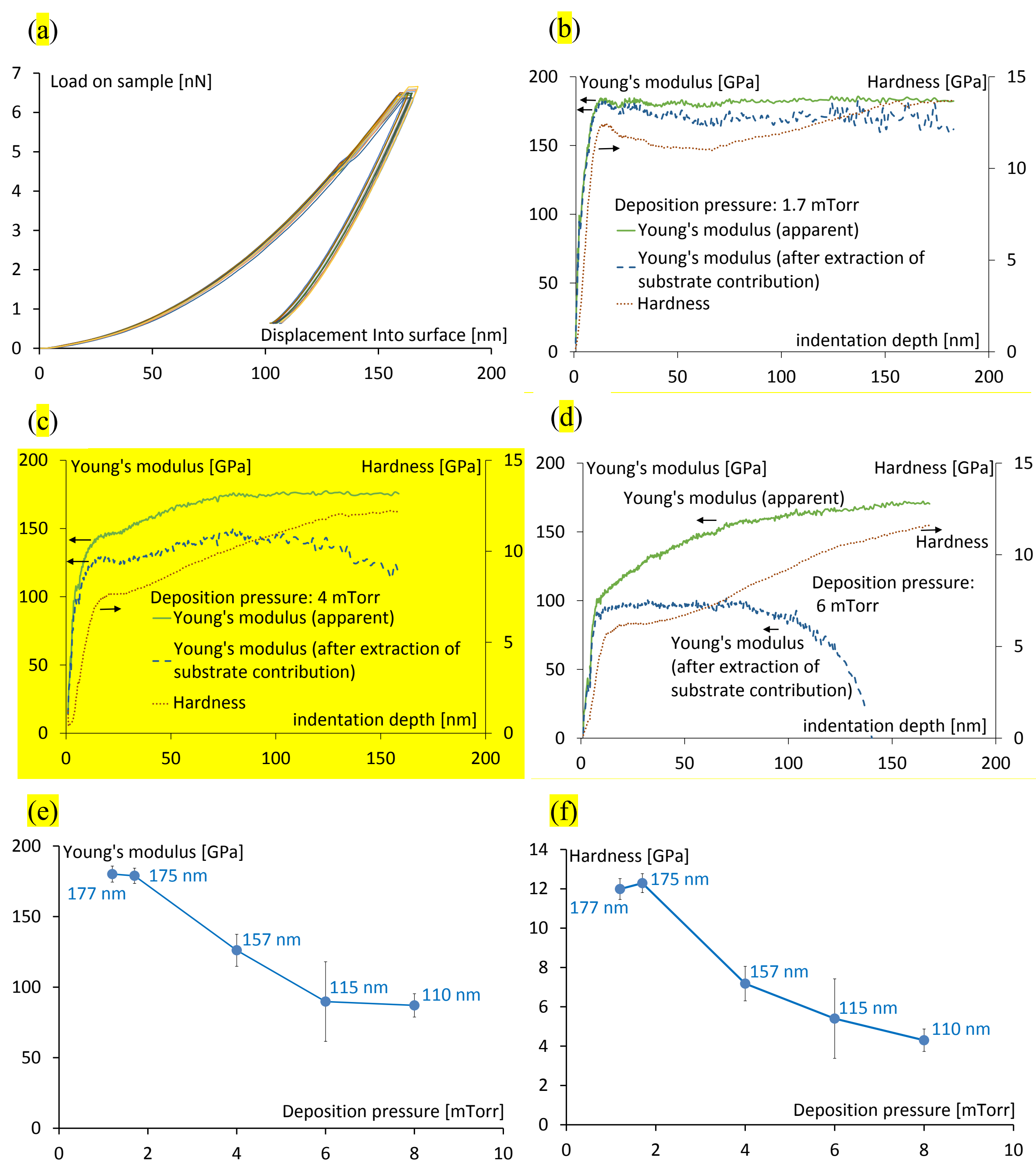

Fig. 5. (a) Variation of the indentation load as function of the displacement into the surface for sixteen indents in the Al_2O_3 thin film deposited at 4 mTorr. (b,c,d) Apparent Young's modulus, Young's modulus computed after subtracting the effect of the substrate and hardness as a function of the indentation depth for Al_2O_3 films deposited at 1.7 mTorr, 4 mTorr and 6 mTorr. (e) Young's modulus and (f) Hardness variation as a function of the deposition pressure for Al_2O_3 films deposited by reactive magnetron sputtering.

Figure(s)

(a)

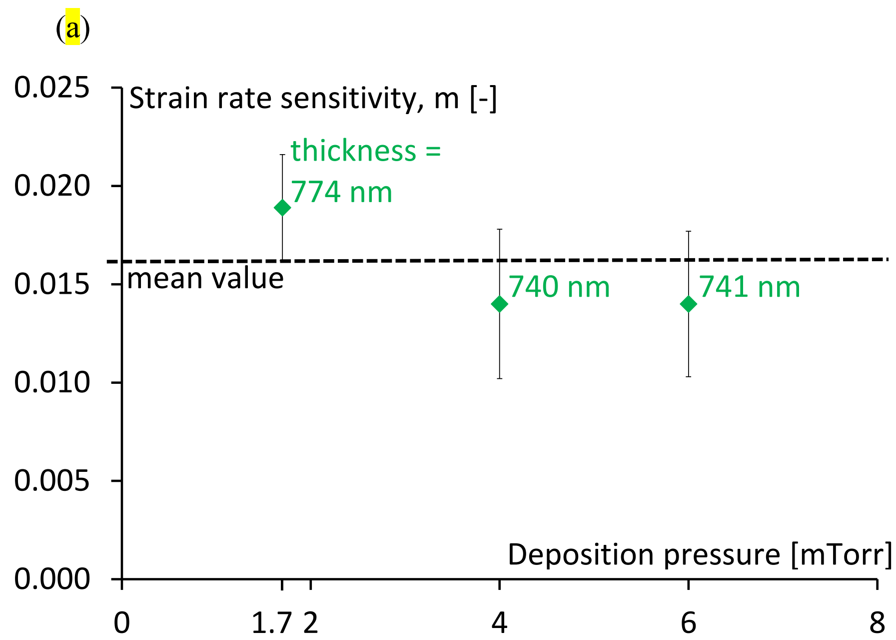

(b)

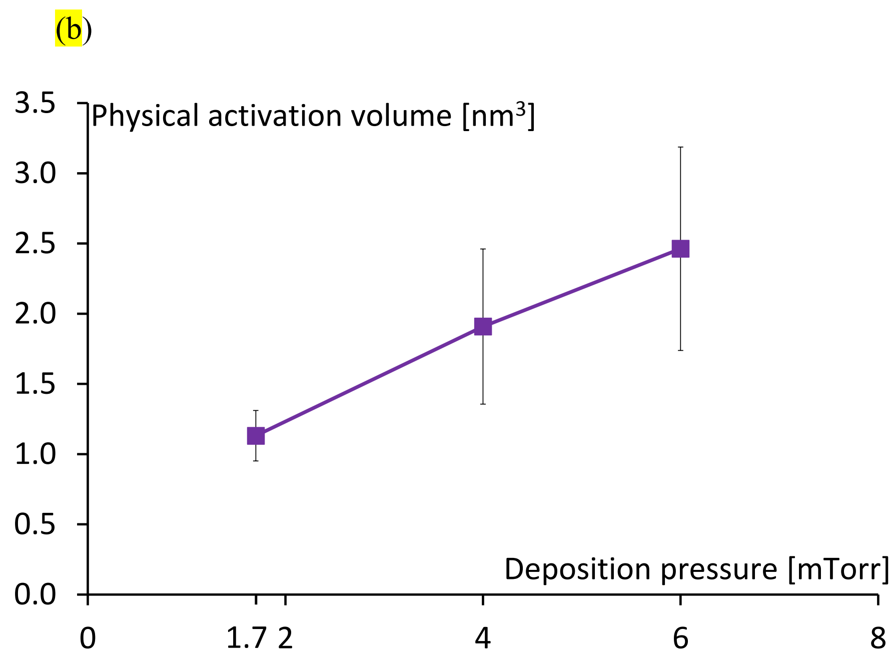

Fig. 6. Variation of the strain rate sensitivity coefficient (a) and physical activation volume (b) as a function of the deposition pressure of sputtered Al_2O_3 thin films.

Figure(s)

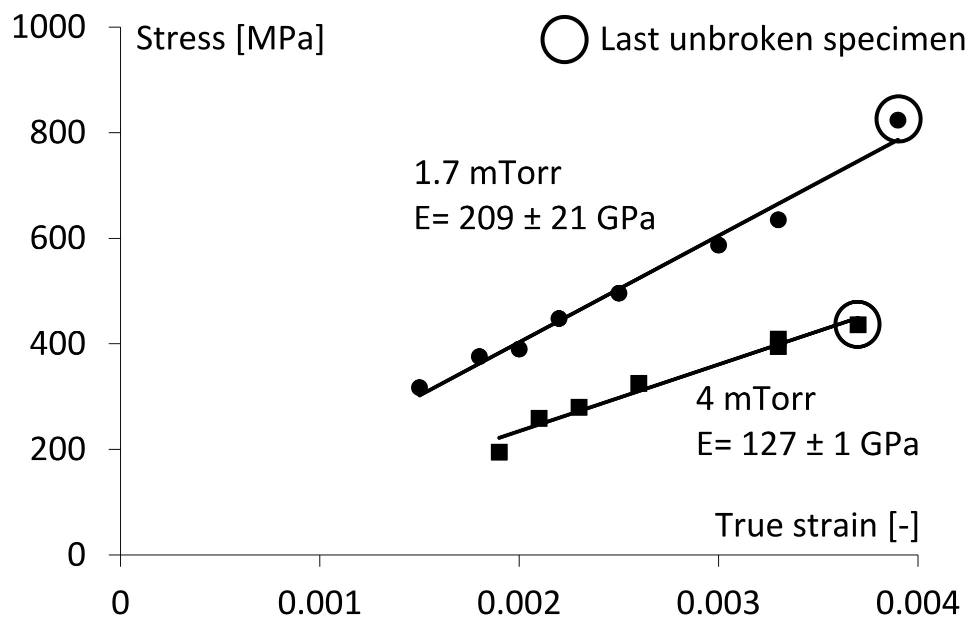

Fig. 7. Stress-strain curves of the Al_2O_3 films deposited at 1.7 mTorr and 4 mTorr, respectively 170 and 220 nm-thick. The Young's modulus is equal to the slope of the linear interpolation.

Figure(s)

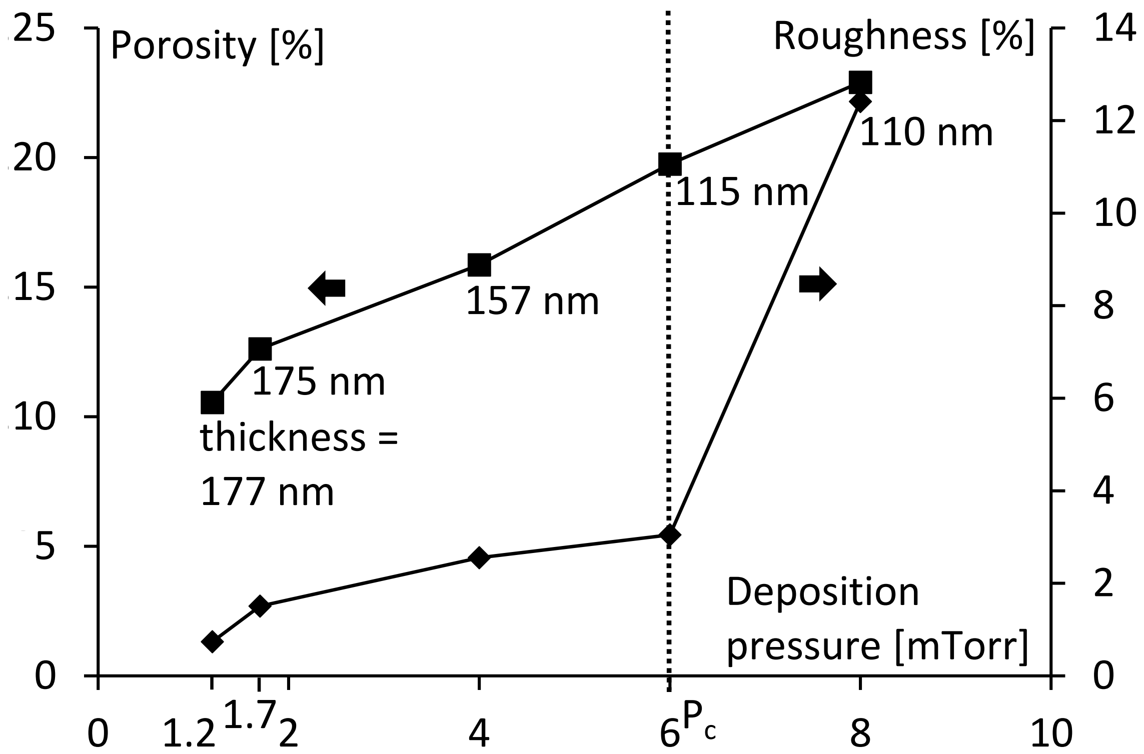

Fig. 8. Variation of the porosity and roughness as a function of the deposition pressure for Al_2O_3 films deposited by reactive magnetron sputtering. The "thermalization pressure" (P_c) is indicated, corresponding to the abrupt increase in the roughness of the films.

Figure(s)

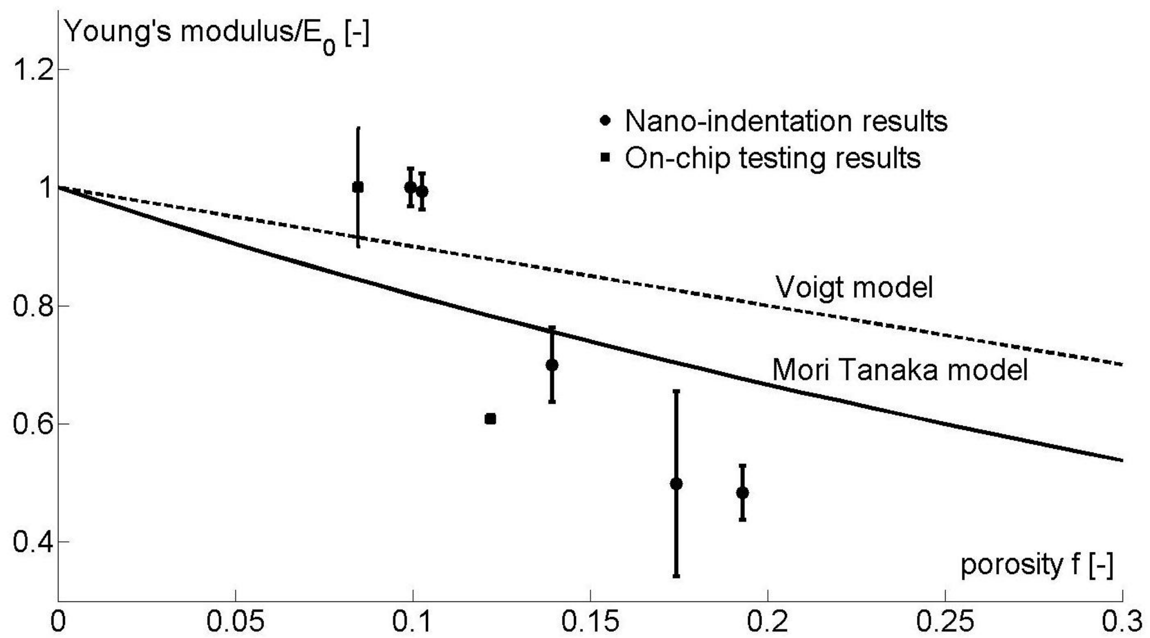

Fig. 9. Variation of the effective normalized Young's modulus as a function of film porosity. Experimental measurements obtained by nanoindentation and by the on-chip testing method are fitted to the models of Mori-Tanaka in the case of spherical voids [44]. The Voigt model prediction is also indicated.

Figure(s)

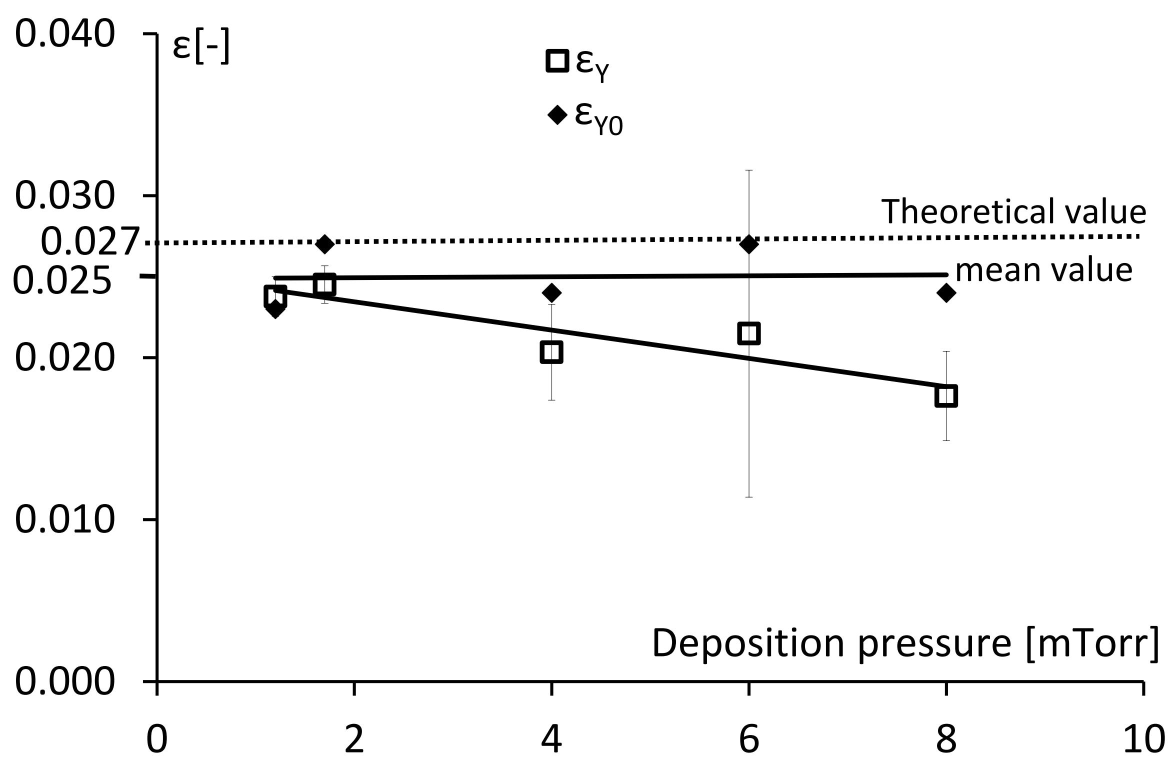

Fig. 10. Variation of the overall strain ε_Y, corresponding to the effective yield stress σ_Y, and strain ε_{Y0} of the alumina matrix surrounding the pores, corresponding to the yield stress σ_{Y0} computed from Gurson model, as a function of the deposition pressure. The average value of ε_{Y0} is 0.025 ± 0.002. The theoretical value for many amorphous materials of 0.027 is also indicated.

Table(s)

Table 1. Average internal stress $< \sigma_f >$ extracted from the substrate curvature change (Fig. 2) and thickness, porosity, roughness and refractive indices n_f, and n_d of the films obtained from ellipsometric measurements.

Deposition pressure [mTorr]	1.2	1.7	4	6	8
$< \sigma_f >$ [MPa]	-15	124	250	353	50
Thickness [nm]	177.5	175.2	156.7	115.0	110.5
Porosity [%]	10.6	12.6	15.9	19.8	22.9
Roughness [nm] (%)	1.3 (0.7)	2.6 (1.5)	3.9 (2.6)	3.4 (3.1)	12.2 (12.4)
Refractive index n_f [-]	1.653	1.650	1.617	1.586	1.570
Refractive index n_d [-]	1.733	1.747	1.738	1.735	1.740

Table(s)

Table 2. Effective Young's modulus (E) and Young's modulus of the dense part of the films E_0 for each deposition pressure, as computed with the Mori-Tanaka model. The porosities used in the model are the values obtained by ellipsometry (Table 1).

Deposition pressure	E from nanoindentation testing [GPa]	E_0 from nanoindentation testing [GPa]	E from on-chip testing [GPa]	E_0 from on-chip testing [GPa]
1.2 mTorr	180	223	/	/
1.7 mTorr	179	231	209	269
4 mTorr	126	174	127	175
6 mTorr	90	134	/	/
8 mTorr	87	139	/	/

Table 3. Effective yield stress σ_Y and the corresponding strain ε_Y, yield stress σ_{Y0} of the alumina matrix surrounding the pores and corresponding strain ε_{Y0} for each deposition pressure computed from Gurson model, using the indicated "Gurson factor" values. The porosities used in the model are the values obtained by ellipsometry (Table 1) and the Young's modulus values are the ones obtained by nanoindentation (Table 2).

Deposition pressure	Hardness [GPa]	"Gurson factor"	Elastic limit σ_Y [GPa]	Elastic limit σ_{Y0} [GPa]	Strain corresponding to ε_Y [-]	Strain corresponding to ε_{Y0} [-]
1.2	12 ± 0.5	2.3	4.28	5.22	0.024	0.023
1.7	12.3 ± 0.5	2	4.39	6.15	0.025	0.027
4 mTorr	7.2 ± 0.9	1.7	2.56	4.23	0.020	0.024
6 mTorr	5.4 ± 2	1.5	1.93	3.6	0.021	0.027
8 mTorr	4.3 ± 0.6	1.3	1.54	3.3	0.018	0.024

*Graphical Abstract

Al_2O_3 thin films microstructure ↔ mechanical properties

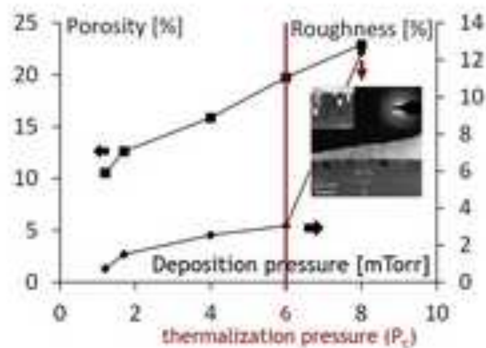

On-chip tensile testing

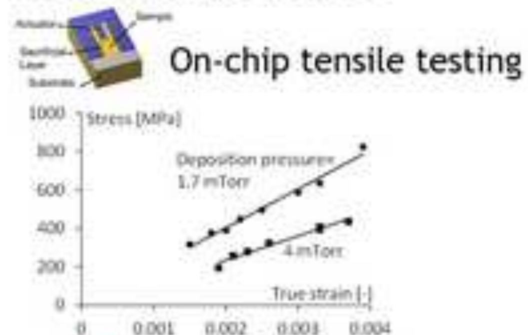

Nanoindentation